

# Role of CeNiSi<sub>2</sub> and BaNiSn<sub>3</sub> Structure Types in the Emergent Magnetism of the Homologous Series Ln<sub>n+1</sub>M<sub>n</sub>X<sub>3n+1</sub>:Ce<sub>4</sub>Fe<sub>3</sub>Ge<sub>10</sub>

Published as part of *Chemistry of Materials* special issue "In Memory of Prof. Francis DiSalvo".

Alexis Dominguez Montero, Sebastian A. Stoian, Gregory T. McCandless, Ryan E. Baumbach, and Julia Y. Chan\*



Cite This: *Chem. Mater.* 2024, 36, 8534–8545



Read Online

ACCESS |



Metrics & More

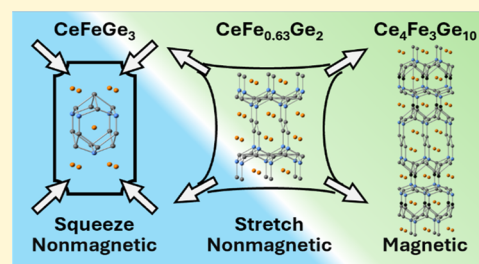


Article Recommendations



Supporting Information

**ABSTRACT:** The synthesis and characterization of Ce<sub>4</sub>Fe<sub>3</sub>Ge<sub>10</sub>,  $n = 3$ , member of the homologous series Ln<sub>n+1</sub>M<sub>n</sub>X<sub>3n+1</sub> (Ln = lanthanides, M = transition metal, X = tetrel), is reported. The structure can be modeled with the *Cmcm* space group adopting the Eu<sub>2</sub>Ni<sub>2-x</sub>Sn<sub>5</sub> structure type, with lattice parameters of  $a = 4.3323$  (15) Å,  $b = 35.507$  (9) Å, and  $c = 4.3069$  (12) Å. Members of the series for  $n > 2$  consist of stacking of ordered (CeNiSi<sub>2</sub> type) and disordered (BaNiSn<sub>3</sub>/AuCu<sub>3</sub> type) subunits with the latter acting as a “spacer” between CeNiSi<sub>2</sub> subunits. Although neither CeFeGe<sub>3</sub> nor CeFe<sub>0.63</sub>Ge<sub>2</sub> order magnetically down to 2 K, Ce<sub>4</sub>Fe<sub>3</sub>Ge<sub>10</sub> is an antiferromagnet below 3.6 K. To rationalize the emergent magnetism: (i) we established the Kondo- and RKKY-interaction dominant regions for the Ce analogues adopting the BaNiSn<sub>3</sub> and CeNiSi<sub>2</sub> by creating an electronic landscape for each and (ii) mapped the strained subunits, due to stacking, within the series. We established that the CeFeGe<sub>3</sub> subunit within Ce<sub>4</sub>Fe<sub>3</sub>Ge<sub>10</sub> contracts and is located within the Kondo-interaction dominant region, while the CeFeGe<sub>2</sub> subunit expands and is in the RKKY-interaction dominant region.



## 1. INTRODUCTION

The stacking sequence of structural motifs for each member of a homologous series provides a platform for systematically studying the structure–property relationships. The number of stacking repeats of a motif and chemical substitutions within the motif can provide a means to produce emergent behavior. A well-known example is Ce<sub>n</sub>MIn<sub>3n+2</sub> ( $n = 1, 2, \infty$ ; M = Co, Rh, Ir), members of the Ln<sub>n</sub>M<sub>m</sub>X<sub>3n+2m</sub> homologous series, which consists of a MIn<sub>2</sub> slabs (PtHg<sub>2</sub> type) and  $n$  slabs of CeIn<sub>3</sub> (AuCu<sub>3</sub> type) along the tetragonal  $c$ -axis.<sup>1</sup> The base unit in the series, CeIn<sub>3</sub> ( $n = 1, m = 0$ ), is a heavy fermion antiferromagnet with commensurate ordering at  $T_N = 10$  K and superconducting at 200 mK with an applied pressure of 25 kbar.<sup>2–4</sup> Among the  $n = 1$  analogues, both CeCoIn<sub>5</sub><sup>5</sup> and CeIrIn<sub>5</sub><sup>6</sup> exhibit unconventional superconductivity with a  $T_c = 2.3$  and 0.4 K under ambient pressure, respectively, while CeRhIn<sub>5</sub> orders antiferromagnetically at 3.8 K, similar to CeIn<sub>3</sub>. In addition, CeRhIn<sub>5</sub> exhibits a dome of superconductivity spanning a quantum critical point with a maximum  $T_c = 2.1$  K at 16 kbar.<sup>5,6</sup> Among the  $n = 2$  analogues, Ce<sub>2</sub>CoIn<sub>8</sub> exhibits superconductivity below  $T_c = 0.4$  K,<sup>7</sup> while Ce<sub>2</sub>MIn<sub>8</sub> (M = Rh, Ir) orders antiferromagnetically at 2.8 K and remains paramagnetic down to 50 mK.<sup>1</sup> The occurrence of superconductivity at ambient pressure for some of the Ce<sub>n</sub>MIn<sub>3n+2</sub> members, compared to the antiferromagnetic order in CeIn<sub>3</sub>, showcases the tunability achieved by

stacking MIn<sub>2</sub> (PtHg<sub>2</sub> type) slabs. Comparing the crystal structure of the ambient pressure superconductors CeCoIn<sub>5</sub> and CeIrIn<sub>5</sub> with the pressure-induced superconductors CeIn<sub>3</sub> and CeRhIn<sub>5</sub> concluded that the stronger distortion of the cuboctahedra (CeIn<sub>3</sub> subunit) may be correlated to superconductivity at atmospheric pressure.<sup>8,9</sup> Compressibility studies of CeMIn<sub>5</sub> and Ce<sub>2</sub>MIn<sub>8</sub> (M = Co, Rh, and Ir) show the stiffening of the lattice with the addition of MIn<sub>2</sub> layers to CeIn<sub>3</sub> while also revealing the ambient pressure  $c/a$  ratio's correlation to the maximized superconducting transition temperature achievable,  $T_c^{\text{max}}$ , in the CeMIn<sub>5</sub> compounds.<sup>10</sup> The Ce<sub>n</sub>MIn<sub>3n+2</sub> (M = Co, Rh, Ir) members of a homologous series thus exemplify how understanding the structural changes between higher-order family members and the subunits can be correlated to the emergent properties.

Our group has discovered a homologous series with the formula Ln<sub>n+1</sub>M<sub>n</sub>X<sub>3n+1</sub> (Ln = lanthanides, M = transition metal, X = tetrel).<sup>11</sup> The series consists of stacking ordered (CeNiSi<sub>2</sub> type) and disordered (BaNiSn<sub>3</sub>/AuCu<sub>3</sub> type) subunits, with

Received: July 12, 2024

Revised: August 14, 2024

Accepted: August 15, 2024

Published: August 27, 2024



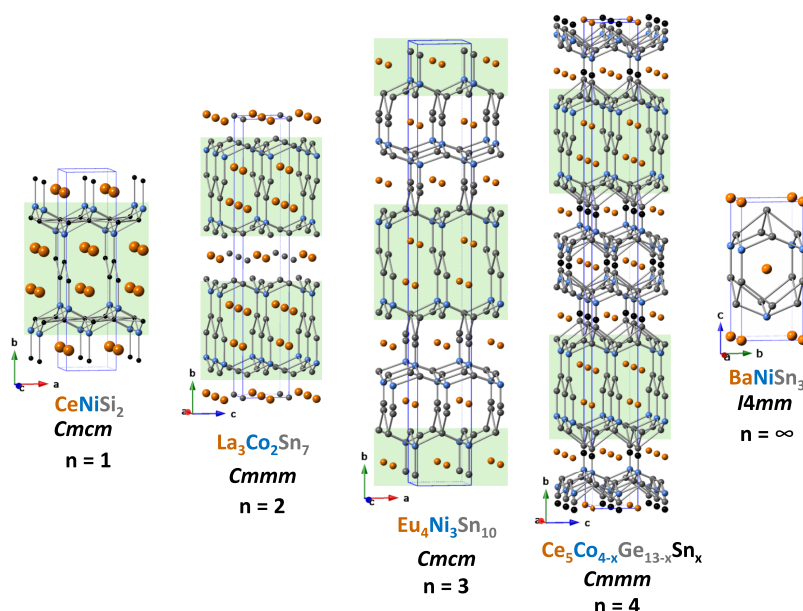


**Figure 1.** Depiction of the intermetallic homologous series  $\text{Ln}_{n+1}\text{M}_n\text{X}_{3n+1}$  ( $\text{Ln}$  = lanthanide,  $\text{M}$  = transition metal, and  $\text{X}$  = tetrel). Green highlights the  $\text{CeNiSi}_2$  slab while the spacing in between is composed of  $\text{BaNiSn}_3/\text{AuCu}_3$  slabs.

the latter subunits acting as a “spacer” between  $\text{CeNiSi}_2$  subunits. There are  $n-1$  ( $\text{BaNiSn}_3/\text{AuCu}_3$  type) subunits per unit cell in the  $\text{Ln}_{n+1}\text{M}_n\text{X}_{3n+1}$  ( $\text{Ln}$  = lanthanide,  $\text{M}$  = transition metal,  $\text{X}$  = tetrel), which adopt the orthorhombic structures ( $\text{Cmcm}$  and  $\text{Cmmm}$  for odd and even  $n$ , respectively, as depicted in Figure 1). Several of the subunits independently host interesting properties, such as superconductivity,<sup>12</sup> zero thermal expansion in the  $\text{CeNiSi}_2$ , vacancy ordered  $\text{Ln}_4\text{MGe}_8$  ( $\text{Ln}$  = Gd, Yb;  $\text{M}$  = Cr–Ni, Ag),<sup>13</sup> and anomalous ferromagnetism in  $\text{CeRuSi}_2$  with non-Fermi liquid behavior in a Kondo lattice<sup>14</sup> in the monoclinic variant of the  $\text{CeNiSi}_2$  type. Pressure-induced superconductivity<sup>15–17</sup> and complex magnetism<sup>18</sup> with the noncentrosymmetric  $\text{BaNiSn}_3$  structure type have also been observed in several Ce-based Co triad germanide members. On the other hand, all of the Fe triads are nonmagnetic Kondo lattice compounds.<sup>19,20</sup>

Several members of the  $\text{Ce}_{n+1}\text{Co}_n\text{Ge}_{3n+1}$  ( $n = 1, 2, 4, 5, 6, 24$  and  $\infty$ , or  $\text{CeCoGe}_3$ ) exhibit highly correlated behavior, with the higher members of the series showcasing complex anisotropic competition between antiferromagnetic and ferromagnetic ground states. To better understand the correlation between the stacking of the  $\text{BaNiSn}_3$  and  $\text{CeNiSi}_2$  subunits and the emergent properties in the series, we opted to synthesize Fe analogues.  $\text{CeFeGe}_3$  is a heavy fermion nonmagnetic Kondo lattice, while  $\text{CeCoGe}_3$  is a heavy fermion with multiple magnetic orderings below  $\sim 25$  K.<sup>18</sup> This work presents the general trends between the Ce-based noncentrosymmetric  $\text{BaNiSn}_3$  and centrosymmetric  $\text{CeNiSi}_2$  subunits by plotting the volume of the unit cell as a function of valence electron count (VEC) and the tuning of the magnetism in the subunits of the homologous series. We were able to (i) identify the regions with distinct ground states (Kondo and Ruderman–Kittel–Kasuya–Yosida (RKKY)-interaction dominant regions),<sup>25</sup> (ii) demonstrate the compounds reaching a quantum critical point or superconductivity are in the crossover region defined in the electronic landscapes for the Ce-based analogues with the  $\text{BaNiSn}_3$  and  $\text{CeNiSi}_2$  structure types.  $\text{Ce}_4\text{Fe}_3\text{Ge}_{10}$  is an antiferromagnet member of

the homologous series  $\text{Ln}_{n+1}\text{M}_n\text{X}_{3n+1}$ , which consists of the stacking of nonmagnetic subunits,  $\text{CeFeGe}_2$  and  $\text{CeFeGe}_3$ . We can rationalize the emergent magnetism by considering the volume and VEC change caused by the lattice mismatch of the subunits when they are stacked in the  $\text{Ln}_{n+1}\text{M}_n\text{X}_{3n+1}$  series. The  $\text{CeFeGe}_3$  subunit decreases its volume and stays in the Kondo dominant regime, while the  $\text{CeFeGe}_2$  crosses over to the magnetic regime through the expansion of the subunit and higher VEC.

## 2. EXPERIMENTAL SECTION

**2.1. Synthesis.**  $\text{Ce}_4\text{Fe}_3\text{Ge}_{10}$  was grown by flux-growth methods using excess Sn flux.<sup>26</sup> The compound can be grown using Ce, Fe, and Ge in a 6:5:16 molar ratio with an excess of 30 mol of Sn; the total reaction mass was 2.73 g. The elements were placed in a 2 mL Canfield alumina crucible<sup>27</sup> and sealed in a fused silica tube under  $\sim 1/3$  atm of Ar. The sealed ampule was placed in a programmable furnace at 300 °C, heated to 1175 °C at 100 °C/h, and dwelled for 48 h, as shown in Figure 2. The furnace was then cooled at a rate of 2

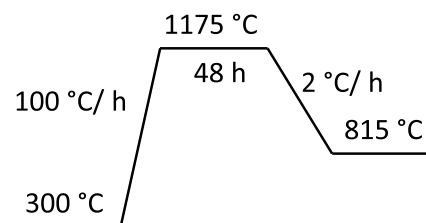


**Figure 2.** Heating profile utilized to synthesize  $\text{Ce}_4\text{Fe}_3\text{Ge}_{10}$ . Reactions with the same reaction ratio were centrifuged at each dwelling temperature to probe whether other members of the series were synthesized. However, all reactions yielded either  $n = 3$  or molten flux.

°C/h to 815 °C, the temperature at which the ampule was rapidly removed, inverted, and centrifuged to remove the excess flux and further etched using 12.1 M  $\text{HCl}:\text{H}_2\text{O}$  in a 1:2 volume ratio. The resulting product was plate-like crystals of  $\text{Ce}_4\text{Fe}_3\text{Ge}_{10}$  (up to 4 mm along the  $a$  and  $c$ -axes) and a minor magnetic impurity ( $\text{Fe}_3\text{Ge}_3$ ), which was mechanically separated. A single plate-like crystal of  $\text{Ce}_4\text{Fe}_3\text{Ge}_{10}$  ( $1 \times 2 \times 4$  mm<sup>3</sup>) was mounted, and X-ray powder

diffraction data was collected along the  $0k0$  direction, as shown in Figure 3, to rule out the intergrowth of other members of the series.

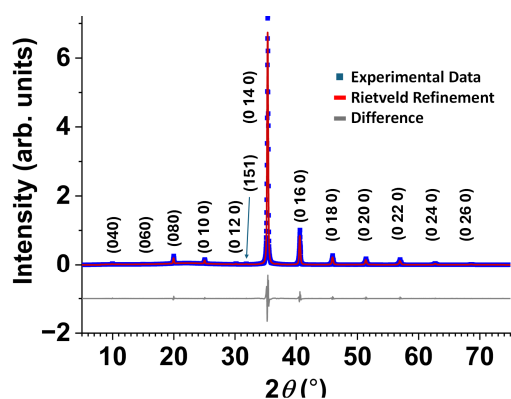


**Figure 3.** X-ray diffraction pattern on a single crystal of  $\text{Ce}_4\text{Fe}_3\text{Ge}_{10}$ . Rietveld refinement was performed considering the preferred orientation. The blue data points correspond to the experimental data, the red line is the Rietveld fit, and the gray line is the difference between both.  $(0k0)$  Bragg peaks observed indicate that the  $[010]$  direction is perpendicular to the large face of the plate-like sample.

Synthesis attempts using the molar ratios 4:3:10, 5:4:13, and 6:5:16 for Ce–Fe–Ge to match those of  $n = 3$ –5 members, normalized to 0.4 g of Ce of the cobalt homologous series, resulted in  $\text{Ce}_4\text{Fe}_3\text{Ge}_{10}$ , where the 6:5:16 ratio yielded the largest crystals. A modified heating profile was also performed, which consisted of the same heating, cooling, and maximum temperature, except the centrifuge temperature was attempted at 1000 and 915 °C. The reaction taken out of the furnace at 1000 °C yielded no crystals since everything was still liquidus, while the sample annealed at 915 °C resulted in small single crystals of  $\text{Ce}_4\text{Fe}_3\text{Ge}_{10}$  ( $<1 \text{ mm}^3$  along the  $a$  and  $c$ -axes).

**2.2. X-ray Diffraction.** A single crystal of  $0.02 \text{ mm} \times 0.03 \text{ mm} \times 0.12 \text{ mm}$  was mounted on a glass fiber by using grease. Data was collected at room temperature using a Bruker D8 Quest Kappa single-crystal X-ray diffractometer with an  $I\mu\text{S}$  microfocus source (Mo  $K\alpha$  radiation,  $\lambda = 0.71073 \text{ \AA}$ ) and a Photon II CPAD area detector. The raw data frames were processed using Bruker SAINT, and multiscan absorption correction was applied using SADABS.<sup>28</sup> A preliminary starting model was obtained utilizing the intrinsic phasing method and SHELXL-2019 for least-squares refinement.<sup>29</sup> In the early stages of the refinement, high residual electronic density was observed between the Fe1 and Ge5 dimer and assigned as Sn5. A refinement considering the sum of the partial occupancies of the Fe1–Ge5 dimer and Sn5 improved the model. Sn was considered instead of Ge due to the bond distance between the excess electronic density and the nearest Ge (Ge3 at  $3.138 \text{ \AA}$ ) being longer than usual Ge–Ge bonds and EDS results indicating Sn is present (see Section 2.4). The resulting bond distance of the Fe1–Ge5 dimer is  $2.296(8) \text{ \AA}$ , similar to the  $2.307 \text{ \AA}$  reported for  $\text{CeFeGe}_3$ .<sup>30</sup> The refined formula corresponds to  $\text{Ce}_4\text{Fe}_{3.23}\text{Ge}_{9.23}\text{Sn}_{0.77}$  and is referred to as  $\text{Ce}_4\text{Fe}_3\text{Ge}_{10}$  for simplicity throughout the article. Table 1 provides the data collection and refinement statistics, and Table 2 provides fractional atomic coordinates.

To confirm the phase purity of multiple single crystals, mechanically separated plate-like crystals were placed on a poly-(methyl methacrylate) (PMMA) sample holder, filling the recess with  $\text{SiO}_2$ . X-ray diffraction of the  $\text{Ce}_4\text{Fe}_3\text{Ge}_{10}$  samples was performed on a Bruker D2 Phaser between  $2\theta = 5$ – $75^\circ$  (Figure 3 shows a diffraction pattern of a single crystal). For single domain confirmation prior to property measurements, a large plate-like crystal of  $\sim 2 \times 3 \times 4 \text{ mm}^3$  was mounted on a glass fiber using low-melting point wax. X-ray backscattering images were obtained utilizing a Photonic Science Laue system (AL048) coupled with a Thermo Kevex DXS-11-5025 X-ray source (W  $K\alpha$  radiation,  $\lambda = 0.71698 \text{ \AA}$ ) and a dual-lens coupled

**Table 1. Crystallographic Data and Refinement Parameters of  $\text{Ce}_4\text{Fe}_{3.23}\text{Ge}_{9.23}\text{Sn}_{0.77}$** <sup>a</sup>

empirical formula	$\text{Ce}_4\text{Fe}_{3.23}\text{Ge}_{9.23}\text{Sn}_{0.77}$
space group, crystal system	$Cmcm$ , orthorhombic
lattice parameters	
$a$ ( $\text{\AA}$ )	4.3323 (15)
$b$ ( $\text{\AA}$ )	35.507 (9)
$c$ ( $\text{\AA}$ )	4.3069 (12)
volume ( $\text{\AA}^3$ )	662.5 (3)
$Z$	2
density ( $\text{g/cm}^3$ )	7.531
absorption coefficient ( $\text{mm}^{-1}$ )	38.79
$F(000)$	1300
crystal size ( $\text{mm}^3$ )	$0.02 \times 0.03 \times 0.12$
$\theta$ range (deg)	2.3–30.5
index range	
$h$	$-6 \rightarrow 6$
$k$	$-50 \rightarrow 50$
$l$	$-6 \rightarrow 6$
number of reflections	11 912
unique reflections	638
data/restraints/parameters	638/0/42
$R_{\text{int}}$	0.080
$\Delta\rho_{\text{max/min}}$	2.23/–3.20
GoF	1.136
$R_1 [F^2 > 2\sigma(F^2)]$	0.040
$wR_2 (F^2)$	0.136
<sup>a</sup> $R_1 = \sum( F_o  -  F_c )/\sum F_o $ and $wR_2 = \{\sum w[(F_o)^2 - (F_c)^2]^2/\sum w[(F_o)^2]^2\}^{1/2}$ .	

**Table 2. Fractional Atomic Coordinates and Displacement Parameters of  $\text{Ce}_4\text{Fe}_{3.23}\text{Ge}_{9.23}\text{Sn}_{0.77}$**

site label	$x$	$y$	$z$	$U_{\text{eq}} (\text{\AA}^2)$	occupancy
Ce1	0	0.81930 (2)	1/4	0.0117 (3)	
Ce2	0	0.54774 (2)	1/4	0.0103 (3)	
Fe1	0	0.72956 (13)	1/4	0.0251 (14)	0.614 (11)
Fe2	0	0.91128 (6)	1/4	0.0085 (5)	
Ge1	0	0.97810 (5)	1/4	0.0099 (4)	
Ge2	0	0.25013 (7)	1/4	0.0284 (6)	
Ge3	0	0.38428 (5)	1/4	0.0113 (4)	
Ge4	0	0.11572 (5)	1/4	0.0112 (4)	
Ge5	0	0.66491 (19)	1/4	0.0176 (10)	0.614 (11)
Sn5	0	0.6800 (2)	1/4	0.0191 (13)	0.386 (11)

Laue camera. The backscattering X-ray collection was performed on the flat surface of the crystal along the  $[010]$ , as shown in Figure S1.

**2.3. Magnetic Properties.** Magnetic properties were measured on a single crystal of 39.9 mg using a Magnetic Properties Measurement System (MPMS). Temperature-dependent magnetic susceptibility ( $\chi = M/H$ ) was measured from 1.8–300 K under an applied magnetic field of  $H = 0.1 \text{ T}$  along each of the principal axes under zero-field cooled (ZFC) and field-cooled (FC) conditions. Field-dependent magnetization isotherm ( $M/H$ ) measured at 1.8 K for  $-7 \text{ T} < H < 7 \text{ T}$ .

**2.4. Energy-dispersive X-ray Spectroscopy.** Energy dispersive X-ray spectroscopy (EDS) was performed on  $\text{Ce}_4\text{Fe}_3\text{Ge}_{10-x}\text{Sn}_x$  through a Versa 3D focused ion beam scanning electron microscope with an acceleration voltage of 20 kV. By normalizing the weight percent to Ce and averaging five spots randomly selected on the crystal, shown in Figure 4, the resulting atomic formula was  $\text{Ce}_4\text{Fe}_{3.28}\text{Ge}_{9.59}\text{Sn}_{0.56}$ , which is in good agreement with the single crystal X-ray diffraction refinement formula ( $\text{Ce}_4\text{Fe}_{3.23}\text{Ge}_{9.23}\text{Sn}_{0.77}$ ).

**2.5. Fe Mössbauer.** The data included in this report were acquired using a spectrometer operated in a constant acceleration

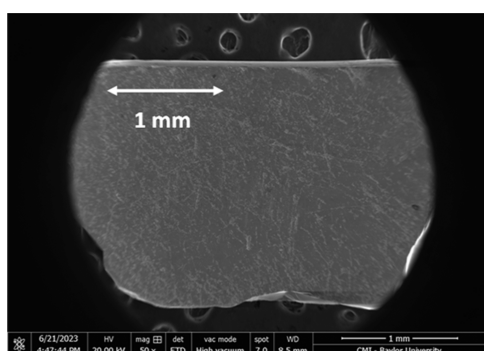


**Figure 4.** Single crystal of  $\text{Ce}_4\text{Fe}_3\text{Ge}_{10}$  utilized for EDS ( $\sim 2 \text{ mm} \times 3 \text{ mm} \times 4 \text{ mm}$ ).

mode. This instrument was equipped with a Janis 8DT cryostat. Spectra recorded at 4.2 K were obtained by submerging the absorber in liquid helium. Isomer shift values are reported with respect to the centroid of a room temperature (RT) spectrum recorded for  $\alpha$ -Fe foil. Theoretical simulations were obtained using the WMOSS spectral simulation software (see Co., formerly Web Research, Edina, MN) as well as C-based Igor Pro codes developed in-house. The absorber was prepared by dispersing  $\sim 30 \text{ mg}$  of ground crystals in eicosane, which functioned as an inert matrix.

**2.6. Heat Capacity and Resistivity.** A Physical Properties Measurement System (PPMS) was used to perform temperature-dependent heat capacity  $C(T)$  and electrical resistivity  $\rho(T)$  measurements in a zero field.  $C(T)$  and  $\rho(T)$  were measured for 1.8–30 and 1.8–350 K, respectively.  $\rho(T)$  measurements were performed using the four-wire method, where platinum wires were spot-welded to the sample such that the electrical current flowed within the  $a$ - $c$  plane.

### 3. RESULTS

**3.1. Structure.**  $\text{Ce}_4\text{Fe}_3\text{Ge}_{10}$  adopts the orthorhombic  $Cmcm$   $\text{Eu}_2\text{Ni}_{2-x}\text{Sn}_5$ <sup>31</sup> structure type with lattice parameters of  $a = 4.3323$  (15) Å,  $b = 35.507$  (9) Å, and  $c = 4.3069$  (12) Å, as shown in Figure 5. The crystallographic data refinement and atomic coordinates are listed in Tables 1 and 2.  $\text{Ce}_4\text{Fe}_3\text{Ge}_{10}$  is the  $n = 3$  member of the  $\text{Ln}_{n+1}\text{M}_n\text{X}_{3n+1}$  ( $\text{Ln} = \text{lanthanide}$ ,  $\text{M} = \text{transition metal}$ ,  $\text{X} = \text{tetrel}$ ) homologous series, where the structure consists of two Ce, two Fe, and six main group element crystallographically distinct sites.  $\text{Ce}_4\text{Fe}_3\text{Ge}_{10}$  can be described as stacking of the structural subunits:  $\text{CeNiSi}_2$ ,  $\text{AuCu}_3$ , and  $\text{BaNiSn}_3$  structure types. Table 3 provides bond distances in  $\text{Ce}_4\text{Fe}_3\text{Ge}_{10}$ ,  $\text{Pr}_4\text{Fe}_3\text{Ge}_{10}$ ,  $\text{CeFeGe}_3$ ,  $\text{CeSn}_3$ ,  $\text{CeGe}_3$ ,  $\text{CeFe}_{0.63}\text{Ge}_2$ , and  $\text{CeGe}_{1.76}$ .

**3.1.1.  $\text{BaNiSn}_3/\text{AuCu}_3$  Subunit.** The Ce1 local environment can be described as a disordered  $\text{BaNiSn}_3/\text{AuCu}_3$  subunit. When the Fe1–Ge5 dimer is present (Figure S2), the local environment of Ce1 adopts the local environment of the lanthanide in the  $\text{BaNiSn}_3$  structure type, with 12 germanium atoms (four Ge2, two Ge3, two Ge4, and four Ge5) and six iron atoms (five Fe1 and one Fe2). The interplanar distance along the  $b$ -axis between the germanium square nets in  $\text{Ce}_4\text{Fe}_3\text{Ge}_{10}$  ( $n = 3$ ) is 4.768 (3) Å, which is also less compared to the reported 4.972 Å in  $\text{CeFeGe}_3$  (Figure S2). The volume of the Ce1-centered polyhedron ( $83.531 \text{ \AA}^3$ ) is reduced by 4.7% in comparison with that of Ce1 in  $\text{CeFeGe}_3$  ( $87.637 \text{ \AA}^3$ ), as shown in Figure S2.

When Sn5 is present, the local environment of Ce1 is a cuboctahedron related to the  $\text{AuCu}_3$  structure type. The cuboctahedron volume in the  $\text{Ce}_4\text{Fe}_3\text{Ge}_{10}$  is  $75.79 \text{ \AA}^3$ , which is

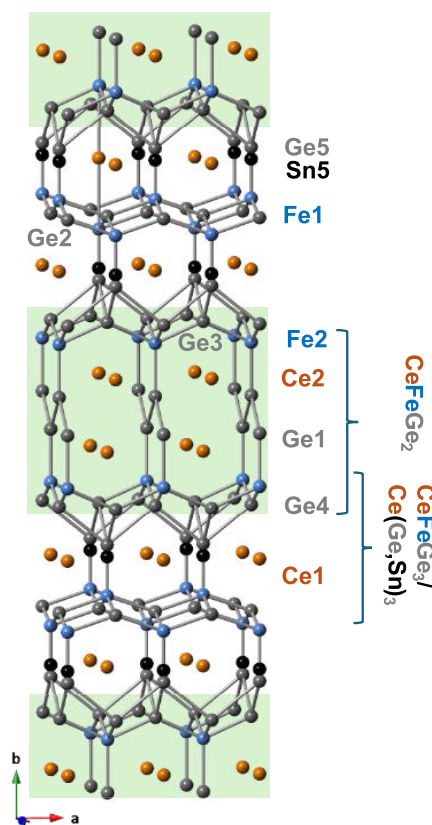


**Figure 5.** Crystal structure of  $\text{Ce}_4\text{Fe}_3\text{Ge}_{10}$  highlighting the  $\text{CeFeGe}_2$  subunit within the structure.

between that of  $\text{CeSn}_3$  ( $87.628 \text{ \AA}^3$ ) and the high-pressure stabilized  $\text{CeGe}_3$  ( $68.38 \text{ \AA}^3$ ).<sup>32</sup>

**3.1.2.  $\text{CeNiSi}_2$  Subunit.** The Ce2 local environment can be described as a  $\text{CeNiSi}_2$  subunit with Ce2 in a trigonal prism arrangement, with 10 germanium (six Ge1, two Ge3, and two Ge4) and four iron atoms (Fe2) surrounding each Ce2 site. The Ce2–Fe2 bond distance in  $\text{Ce}_4\text{Fe}_3\text{Ge}_{10}$  is 3.383 (1) Å, longer than that in  $\text{CeFe}_{0.63}\text{Ge}_2$  (3.224 Å). The shortest Ce–Ce distances in  $\text{CeFe}_{0.63}\text{Ge}_2$  are 4.167 Å and 4.170 Å, we observe a contraction and expansion for Ce2–Ce distance within  $\text{Ce}_4\text{Fe}_3\text{Ge}_{10}$  (4.016 (1) Å and 4.3069 (12) Å) (Figure S3). Overall, there is a 4.3% volume expansion of the Ce2 local environment ( $73.685 \text{ \AA}^3$ ) in  $\text{Ce}_4\text{Fe}_3\text{Ge}_{10}$  compared to that of  $\text{CeFe}_{0.63}\text{Ge}_2$  ( $70.678 \text{ \AA}^3$ )<sup>21</sup> as shown in the highlighted section of Figure S3. The expansion of the Ce2 local environment may be the cause of the full occupancy of Fe in comparison with  $\text{CeFe}_{0.63}\text{Ge}_2$ .

The reduction of the Ce1 and expansion of the Ce2 local environments in  $\text{Ce}_4\text{Fe}_3\text{Ge}_{10}$  in comparison to the tetragonal  $\text{CeFeGe}_3$  and orthorhombic  $\text{CeFe}_{0.63}\text{Ge}_2$  could accommodate the lattice mismatch between the latter. The square  $ab$ -plane of  $\text{CeFeGe}_3$  is 4.329 Å by 4.329 Å, while the rectangular  $ab$ -plane of  $\text{CeFe}_{0.63}\text{Ge}_2$  is 4.285 Å by 4.170 Å, ranging between a  $\sim 1$ –4% difference along each axis. Volume expansion and compression of subunits to compensate for the mismatch in lattice parameters of reported prototypes are also observed in the  $\text{Ca}_2\text{Pt}_7\text{XP}_{3-x}$  ( $\text{X} = \text{Al, Ti, Zn}$ ) compounds adopting the  $\text{Eu}_2\text{Pt}_7\text{AlP}_{3-x}$  structure type<sup>33,34</sup> and is analogous to strain engineering.<sup>35</sup>  $\text{Ca}_2\text{Pt}_7\text{XP}_{3-x}$  ( $\text{X} = \text{Al, Ti, Zn}$ ) consists of stacking  $\text{CaBe}_2\text{Ge}_2$  subunits with  $\text{AuCu}_3$ . Both ternary  $\text{CaPt}_2\text{P}_{2-x}$  and binary intermetallic compounds  $\text{XPt}_3$  ( $\text{X} =$

Table 3. Selected Interatomic Distances (Å) in Ce<sub>4</sub>Fe<sub>3</sub>Ge<sub>10</sub> and Related Structures

Ln1 BaNiSn <sub>3</sub> subunit	Ce <sub>4</sub> Fe <sub>3</sub> Ge <sub>10</sub>	Pr <sub>4</sub> Fe <sub>3</sub> Ge <sub>10</sub>	CeFeGe <sub>3</sub>	CeSn <sub>3</sub>	CeGe <sub>3</sub>
Ln1–Ln1	4.3069 (12)	4.2982 (15)	4.329	4.72	4.3485
Ln1–Ln1	4.3323 (15)	4.3207 (10)			
Ln1–Fe1	3.186 (5)	3.227 (4)	3.306		
Ln1–Fe2	3.266 (3)	3.270 (2)			
Ln1–Sn5	3.0545 (7)	3.0473 (6)		3.3375	3.0775
Fe1–Ge2	2.2710 (18)	2.2735 (15)	2.3386		
Fe1–Ge2	2.2862 (18)	2.2862 (13)			
Fe1–Ge5	2.296 (8)	2.259 (5)	2.3071		
Fe2–Ge4	2.3573 (13)	2.3496 (10)	2.3386		
Ln2 CeFeGe <sub>2</sub> subunit	CeFe <sub>0.63</sub> Ge <sub>2</sub>	CeGe <sub>1.76</sub>			
Ln2–Ln2	4.0163 (9)	3.9949 (10)	4.1670	4.1233	
Ln2–Ln2	4.3069 (12)	4.2982 (15)	4.1700	4.2100	
Ln2–Fe2	3.3832 (12)	3.3724 (9)	3.2245	3.2117	
Ln2–Ge1	3.1892 (9)	3.1805 (7)	3.1829	3.2117	
Ln2–Ge4	3.2433 (15)	3.2254 (10)	3.1436	3.148	

Al,<sup>36</sup> Ti,<sup>37</sup> Zn<sup>38</sup>) have previously been reported and have a lattice mismatch of ~4% between their shortest dimension.

**3.2. Mössbauer Spectroscopy.** The zero-field Mössbauer spectra recorded for Ce<sub>4</sub>Fe<sub>3</sub>Ge<sub>10</sub> exhibit an asymmetric quadrupole doublet. At room temperature, this doublet is characterized by an apparent isomer shift  $\delta = 0.40$  mm/s, quadrupole splitting  $\Delta E_Q = 0.40$  mm/s and unequal linewidths  $\Gamma_{L/R} = 0.27/0.35$  mm/s (Figure 6 and Table 4). Lowering the

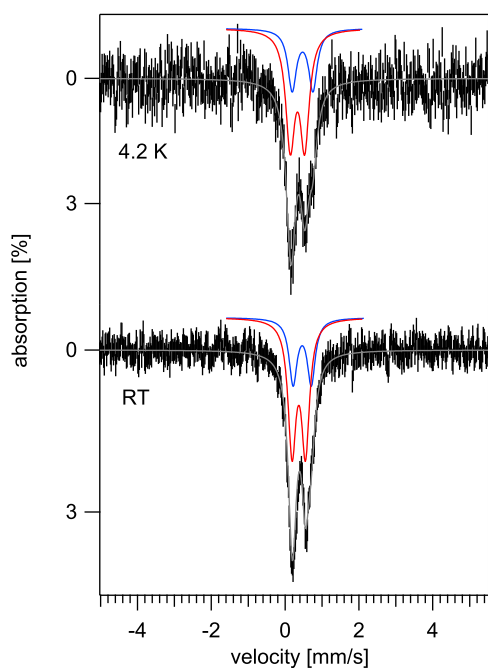


Figure 6. Zero-field Mössbauer spectra recorded for Ce<sub>4</sub>Fe<sub>3</sub>Ge<sub>10</sub> at 4.2 K (top) and room temperature (bottom). The solid gray lines are the theoretical spectra obtained from the sum of two spectral components shown in blue and red above the corresponding experimental spectrum derived using the parameters listed in Table 4.

temperature leads to a small increase in the  $\Delta E_Q$  value and to a slight decrease in the isomer shift, which can likely be traced to a second-order Doppler effect. The persistence of the quadrupole splitting even at 4.2 K, as opposed to the onset of a spontaneous magnetic hyperfine splitting such as that observed previously for Pr<sub>4</sub>Fe<sub>3</sub>Ge<sub>10</sub>,<sup>39</sup> suggests that for

Ce<sub>4</sub>Fe<sub>3</sub>Ge<sub>10</sub> the iron sites either do not contribute to the magnetic ordering observed at low temperature or that their contribution is insignificant. Considering that the structural investigation of Ce<sub>4</sub>Fe<sub>3</sub>Ge<sub>10</sub> revealed the presence of this species of two distinct iron sites, we have simulated these spectra by considering two spectral components with a 1:2 relative ratio, as predicted by the X-ray diffraction data. This procedure led to parameters that, when considering the S/N, are essentially identical to those derived for Pr<sub>4</sub>Fe<sub>3</sub>Ge<sub>10</sub>, as shown in Table 4. Similarly, the larger isomer shift of the minority component, shown in blue, suggests that for these sites, we observe lower s-electron density at the nucleus, when compared to those of the majority component, likely due to an increase in the population of iron's 3d band.

Similarly, the larger quadrupole splitting of the minority component is likely caused by a change in the population of the iron 3d orbitals as opposed to a dramatic difference in the symmetry of the first coordination spheres of the iron sites.

**3.3. Magnetic Susceptibility and Magnetization.** Figure 7 shows the temperature-dependent magnetic susceptibility with  $H = 0.1$  T applied along each of the principal axes. It is evident the  $c$ -axis is the easy axis, while  $\chi(T)$  for  $H//a$  and  $b$  closely resemble each other. This is noteworthy given that the  $ac$  plane is more symmetric than the  $ab$  or  $cb$  planes, which naively might be expected to result in strong magnetic anisotropy between the  $ab$  and  $c$ -directions. Fits to the data using the formula  $1/\chi = (T - \theta_{CW})/C$  (Figure 7a) yield Curie–Weiss constants ( $\theta_{CW}$ ) of  $-118.6$ ,  $-179.8$ , and  $-29.3$  K for the  $a$ ,  $b$ , and  $c$ -axes, respectively. This anisotropy resembles what is seen for Pr<sub>4</sub>Fe<sub>3</sub>Ge<sub>10</sub>,<sup>39</sup> suggesting that the large  $\theta_{CW}$  values for  $H//a$  and  $b$  are due to structural factors that lead to the directions being the magnetically hard axes. In contrast, the smaller negative value for  $H//c$  likely represents the intrinsic antiferromagnetic spin-exchange interactions resulting from Ruderman–Kittel–Kasuya–Yosida (RKKY) interactions. Note that no diamagnetic constant was necessary to describe the magnetic susceptibility above 150 K for fits along the  $c$ -axis, while  $\chi_0 = 2.6$  and  $5$  ( $10^{-4}$  cm<sup>3</sup>/mol Ce) were used for the  $a$ - and  $b$ -directions. Finally, using the formula  $\mu_{\text{eff}} = \sqrt{8C}$ , the effective magnetic moments ( $\mu_{\text{eff}}$ ) along the  $a$ ,  $b$ , and  $c$ -axes are calculated to be 2.54, 2.57, and 2.55  $\mu_B/\text{Ce}$ , respectively. This is similar to the 2.54  $\mu_B/\text{Ce}$  Hund's rule value for trivalent Ce and agrees with the Fe Mössbauer. Antiferromagnetic ordering is seen at  $T_N = 3.6$ – $3.8$  K along all measured directions. The

**Table 4.** Parameters Derived from the Analysis of the Zero-field Mössbauer Spectra Recorded for  $\text{Ce}_4\text{Fe}_3\text{Ge}_{10}$  and Their Comparison to Those Previously Reported for  $\text{Pr}_4\text{Fe}_3\text{Ge}_{10}$

compound	model	temp. [K]	site	$\delta$ [mm/s]	$\Delta E_Q$ [mm/s]	$\Gamma_{L/R}$ [mm/s]	rel. area [%]	ref.
$\text{Ce}_4\text{Fe}_3\text{Ge}_{10}$	1-site	4.2	n.a.	0.37	0.43	0.30/0.40	100	this work
		293	n.a.	0.40	0.40	0.27/0.35	100	
	2-site	4.2	red	0.33	0.39	0.30	66	
			blue	0.47	0.56	0.28	33	
		293	red	0.37	0.36	0.26	66	
			blue	0.46	0.49	0.26	33	
$\text{Pr}_4\text{Fe}_3\text{Ge}_{10}$	1-site	298	n.a.	0.38	0.38	0.29/0.35	100	39
	2-site	298	red	0.37	0.38	0.28	66	
			blue	0.45	0.48	0.28	33	

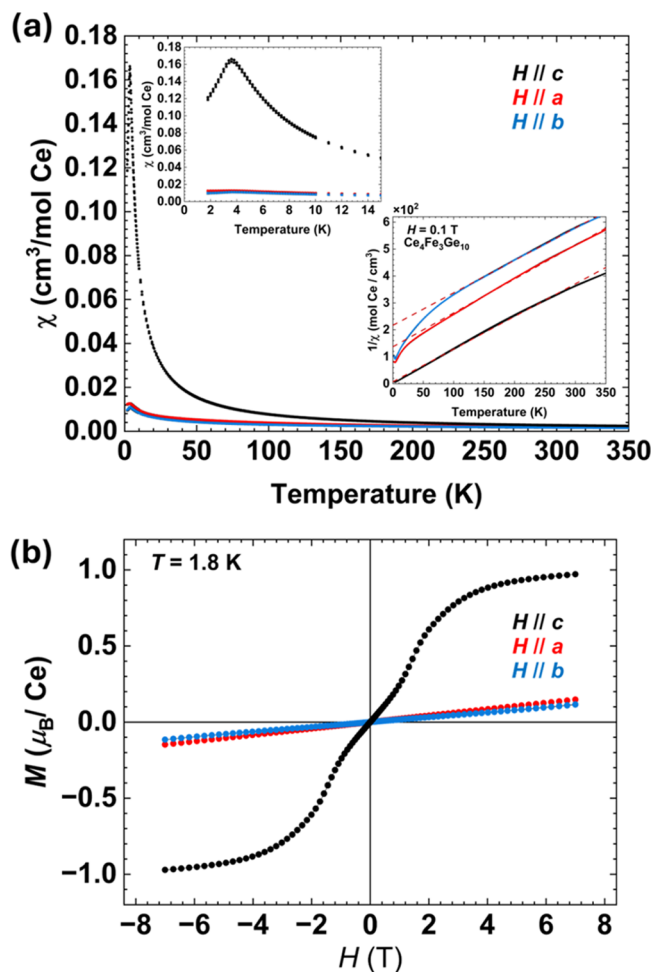


**Figure 7.** (a) Magnetic susceptibility as a function of temperature under 0.1 T. The inset contains a zoomed-in region of the magnetic susceptibility to highlight the ordering and the inverse magnetic susceptibility fit to the Curie–Weiss law (red dashed lines) between each axis. All axes have a magnetic ordering temperature  $T_N = 3.6$ – $3.8$  K. (b) Magnetization as a function of applied field parallel along the principal axes at 1.8 K from  $-7$  to  $7$  T. The  $H//c$  (black circles) is highly anisotropic in comparison with the  $a$  (red circles) and  $b$  (blue circles) axes.

negative values for  $\theta_w$  suggest dominantly antiferromagnetic behavior along all axes, where it is noteworthy that  $T_N \ll \theta_{CW}$  for  $H//c$ , suggesting some degree of magnetic frustration.

As shown in Figure 7b, isothermal magnetization was measured along the principal axes at 1.8 K.  $M(H)$  is strongly anisotropic, where a weak linear increase is seen for  $H//a$  and

$b$ . This is consistent with the spins being resistant to alignment in this direction, as seen in  $\chi(T)$ . In contrast,  $M(H)$  for  $H//c$  increases rapidly with increasing field and shows an abrupt increase near  $H = 1.3$  T due to a metamagnetic phase transition. At large fields,  $M(H)$  for  $H//c$  saturates toward  $0.9 \mu_B/\text{Ce}$ . This value is reduced from the value expected for a full  $\text{Ce}^{3+}$  multiplet, indicating that either crystal electric field splitting or Kondo hybridization reduces the low-temperature magnetic moment.

**3.4. Heat Capacity and Resistivity.** Figure 8a summarizes the temperature dependence of the heat capacity divided

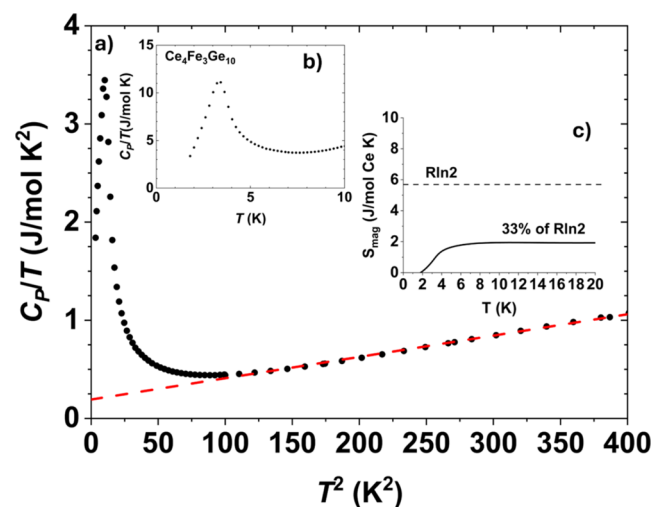


**Figure 8.** (a) Temperature-dependent heat capacity for  $\text{Ce}_4\text{Fe}_3\text{Ge}_{10}$ . A peak at 3.44 K can be observed through the heat capacity, coinciding with the magnetic transition temperature observed through the magnetic susceptibility. (b) The Sommerfeld coefficient for  $\text{Ce}_4\text{Fe}_3\text{Ge}_{10}$  is  $192 \text{ mJ/mol K}^2$ , corresponding to  $48 \text{ mJ/mol Ce K}^2$ . (c) Temperature-independent entropy of the Ce 4f electrons.

by the temperature  $C_p/T$  of  $\text{Ce}_4\text{Fe}_3\text{Ge}_{10}$ . The data are dominated by phonon contribution above 10 K, where a fit to the data using the expression  $\frac{C}{T} = \gamma + \beta T^2$  is shown in Figure 8b, which yields a phononic coefficient  $\beta$  of  $2.17 \text{ mJ/mol K}^2$  and an electronic heat capacity coefficient  $\gamma$  of  $192 \text{ mJ/mol K}^2$ . The latter corresponds to a Sommerfeld coefficient of  $48 \text{ mJ/mol Ce K}^2$ . While this value is not larger by comparison to prototypical heavy fermion materials such as  $\text{CeCoIn}_5$  ( $\gamma = 290 \text{ mJ/mol K}^2$ ),<sup>5</sup> it is nonetheless enhanced by comparison to that of a weakly correlated metal such as copper ( $\gamma = 1 \text{ mJ/mol K}^2$ ). By subtracting the fit to  $C_p/T$  and further integrating  $C_p/T$ , we obtain temperature-dependent entropy  $S_{\text{mag}}$  (Figure 8c),

which reaches 1/3 Rln2 per Ce. Therefore, the values for  $\gamma$  and  $S_{\text{mag}}$  indicate the presence of strong Kondo lattice hybridization. Finally, a lambda-like peak is seen near  $T_N = 3.4$  K. This is consistent with the  $\chi(T)$  measurements, showing the occurrence of an antiferromagnetically ordered ground state.

The temperature-dependent electrical resistivity,  $\rho(T)$ , for electrical current applied in the  $a$ - $c$  plane is shown in Figure 9.

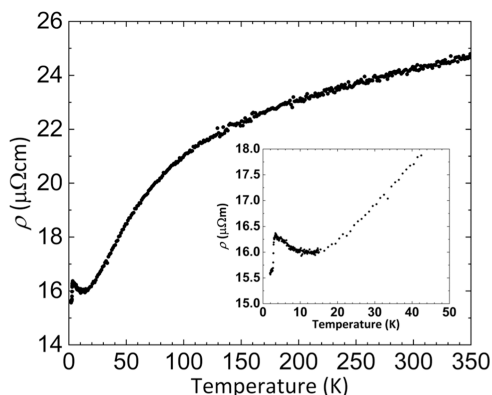


**Figure 9.** Temperature-dependent electrical resistivity of  $\text{Ce}_4\text{Fe}_3\text{Ge}_{10}$  along the  $a$ - $c$  plane. The inset shows the low-temperature region ( $<50$  K), where the ordering temperature is observed.

The RRR is 1.59, which could be due to the structural disorder present in  $\text{Ce}_4\text{Fe}_3\text{Ge}_{10}$ . Similar to what has been seen for several other Ce-based materials in this family, the behavior is typical of a Kondo lattice compound. In particular,  $\rho$  exhibits metallic behavior but initially only weakly decreases with decreasing  $T$ . It eventually evolves through a broad shoulder around 70–80 K as the Kondo coherent state forms at low  $T$ . This is followed by a weak increase that spans from 12 to 4 K and finally an abrupt decrease at  $T_N = 3.4$  K where spin scattering of conduction electrons is removed as the system transitions from paramagnetism to antiferromagnetic order. It is noteworthy that the residual resistivity below the phase transition remains relatively large, indicating the presence of static disorder scattering, which is likely due to structural defects.

## 4. DISCUSSION

**4.1. Magnetic Data.** In the following, we compare  $\text{Ce}_4\text{Fe}_3\text{Ge}_{10}$  with the properties of prototypes  $\text{CeFeGe}_3$  and  $\text{CeFe}_{0.63}\text{Ge}_2$  reported in the literature.  $\text{CeFeGe}_3$  is a concentrated heavy fermion Kondo compound with  $\text{Ce}^{3+}$  valency ( $\mu_{\text{eff}} = 2.57 \mu_B$ ) down to 0.5 K and  $\gamma = 150$  mJ/mol  $\text{K}^2$ .<sup>19</sup>  $\text{CeFe}_{0.63}\text{Ge}_2$  is a heavy fermion compound with Kondo-lattice behavior with  $\gamma = 240$ – $320$  mJ/mol  $\text{K}^2$ .<sup>40</sup>  $\text{Ce}_4\text{Fe}_3\text{Ge}_{10}$  orders antiferromagnetically ( $T_N \sim 3.7$  K) with  $\gamma = 48$  mJ/(mol Ce  $\text{K}^2$ ).<sup>40</sup> To interpret rationalizing the emergent magnetism in  $\text{Ce}_4\text{Fe}_3\text{Ge}_{10}$  compared to  $\text{CeFeGe}_3$  and  $\text{CeFe}_{0.63}\text{Ge}_2$ , we define the ground states of Ce-based analogues of the  $\text{BaNiSn}_3$  and  $\text{CeNiSi}_2$  structure types by plotting the volume of the unit cell as a function of VEC.

**4.1.1.  $\text{BaNiSn}_3$  Electronic Landscape.** To clarify the electronic and magnetic behavior that is seen in the homologous series, we have compiled the reported lattice parameters and properties for the  $\text{CeMX}_3$  ( $M = \text{Groups 8–10}$ ,  $X = \text{Si, Ge}$ ),<sup>15–18,30,41–52</sup> and the  $\text{CeMX}_2$  ( $M = \text{Groups 8–11}$ ,  $X = \text{Si, Ge, Sn}$ )<sup>12,21,40,53–73,74,77</sup> adopting the  $\text{BaNiSn}_3$  (Figure 10), and  $\text{CeNiSi}_2$  structure types (Figure 11), respectively. In

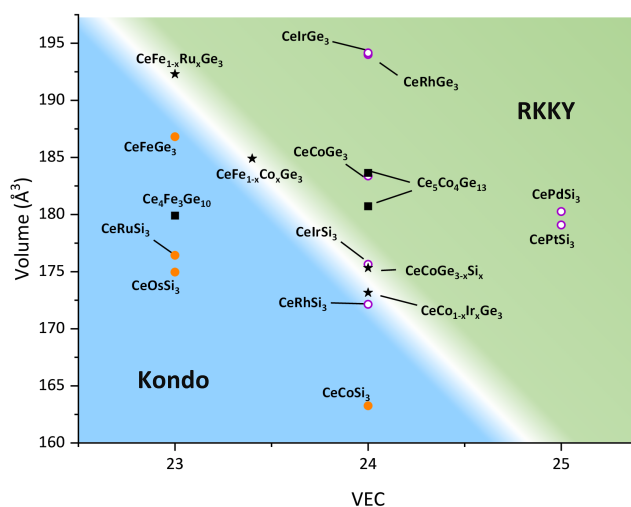


**Figure 10.** Electronic landscape highlighting the competition between Kondo- (blue) and RKKY-interaction (green) dominant regions in the Ce analogues of the  $\text{BaNiSn}_3$  structure type by plotting the volume as a function of the valence electron count (VEC). Within the graph, we have plotted the compounds with Kondo- (orange circle), RKKY-interaction dominant (white circles), near a quantum critical point (star) ground state, and the  $\text{CeMX}_3$  subunits with the homologous series  $\text{Ce}_{n+1}\text{M}_n\text{X}_{3n+1}$  (rectangles).

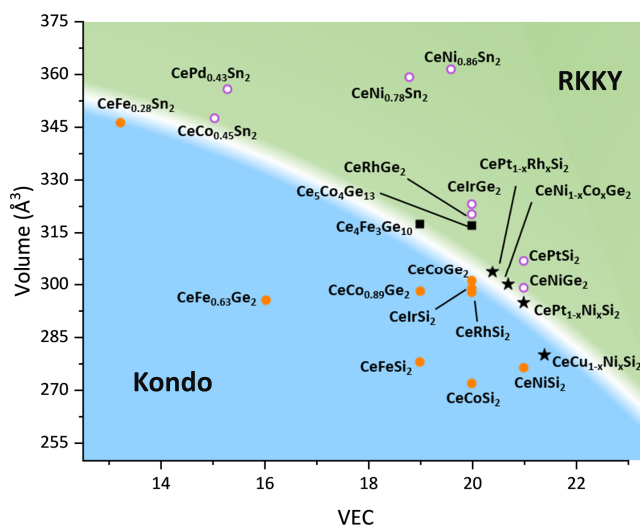


**Figure 11.** Electronic landscape highlighting the competition between RKKY- (green) and Kondo-interaction dominant (blue) in the Ce analogues of the  $\text{CeNiSi}_2$  structure type by plotting the volume as a function of valence electron count (VEC). Within the graph, we have plotted compounds with the Kondo- (orange circle), RKKY-interaction dominant (white circles), near a quantum critical point (star) ground states, and the subunits of the homologous series (rectangles).

particular, the electronic and magnetic behaviors are plotted in the space defined by the unit cell volume and the valence electron count (VEC). For both the  $\text{CeMX}_3$  and  $\text{CeMX}_2$  compounds, three regions can be delineated within the electronic landscape: (i) the bottom left region (blue) is composed of compounds where Kondo interactions are dominant (orange circle), (ii) the top right (green) is composed of compounds where RKKY interactions are dominant, having magnetic ordering, (white circle) and (iii)

the crossover region (white) is composed of compounds associated with magnetic quantum criticality and, in some cases, superconductivity. Further details regarding Kondo and RKKY interactions with a Doniach diagram (Figure S4) are provided in the Supporting Information. The crossover region for  $\text{CeMX}_3$  can be validated by plotting the doping studies (stars) of  $\text{CeFe}_{1-x}\text{Ru}_x\text{Ge}_3$ ,<sup>78</sup>  $\text{CeFe}_{1-x}\text{Co}_x\text{Ge}_3$ ,<sup>79–81</sup>  $\text{CeCo}_{1-x}\text{Ir}_x\text{Si}_3$ ,<sup>44</sup> and  $\text{CeCoGe}_{3-x}\text{Si}_x$ ,<sup>82,83</sup> each of which is driven toward a quantum critical point (QCP) at particular  $x$  values. Similar to what is seen for other prototypical Kondo lattice antiferromagnetic quantum critical points such as the pressure-tuned  $\text{CeRhIn}_5$ ,<sup>84</sup> we also observe that the Sommerfeld coefficient goes through a maximum for compounds closer to the crossover region, as expected when approaching a QCP.<sup>85</sup> Such observation is consistent with the enhancement of the Sommerfeld coefficient when near a QCP in the doping study of  $\text{CeFe}_{1-x}\text{Ru}_x\text{Ge}_3$ .<sup>78,85</sup> Figure 10 thus reveals the importance of tuning both the unit cell volume and VEC to reach regions with interesting properties, similar to what was previously observed of the Ce analogues of the  $\text{ThCr}_2\text{Si}_2$  structure type.<sup>86</sup>

This result is consistent with those of earlier studies. For example, Sun et al. correlated the ambient pressure volume with the critical pressure and maximum superconductivity temperature ( $T_c^{\text{max}}$ ) for  $\text{CeMX}_3$  ( $M = \text{Co, Rh, Ir}$  and  $X = \text{Si, Ge}$ ).<sup>17</sup> This work found (i) the critical pressure to achieve  $T_c^{\text{max}}$  is correlated nonlinearly to the initial volume; (ii) the estimated unit cell volume at which  $T_c^{\text{max}}$  is achieved is within a narrow range ( $V \sim 168\text{--}175 \text{ \AA}^3$ ); and (iii)  $T_c^{\text{max}}$  is correlated to spin–orbit coupling.<sup>17</sup> In Figure 10, we observe (i) the distance between the Co triad compounds and the crossover regime, in a vertical path where the VEC is unchanged, is correlated nonlinearly to the pressure necessary to realize superconductivity; (ii) the estimated volume of the isoelectronic compounds based on Vegard's law,  $\text{CeCoGe}_{3-x}\text{Si}_x$  ( $x = 1.25$ ) and  $\text{CeCo}_{1-x}\text{Ir}_x\text{Si}_3$  ( $x = 0.35$ ), which are near a QCP and superconduct, respectively, are between  $173\text{--}175 \text{ \AA}^3$ . Therefore, we have reached the same conclusion as Sun et al., while exposing additional regions of interest with distinct VECs.

These results also clarify the behavior in the homologous series. As mentioned before, due to the mismatch of the subunits' lattice parameters, we see a contraction and expansion of the  $\text{CeFeGe}_3$  and  $\text{CeFeGe}_2$  subunits, respectively. The hypothetical unit cell volume of the  $\text{CeFeGe}_3$  and  $\text{CeCoGe}_3$  subunits within  $\text{Ce}_4\text{Fe}_3\text{Ge}_{10}$  ( $179.90 \text{ \AA}^3$ ) and  $\text{Ce}_5\text{Co}_4\text{Ge}_{13}$  ( $180.73$  and  $183.66 \text{ \AA}^3$ )<sup>22</sup> showcase such contraction. Note that  $\text{Ce}_5\text{Co}_4\text{Ge}_{13}$  has two distinct crystallographic sites with disordered  $\text{BaNiSn}_3/\text{AuCu}_3$  subunit and therefore has two data points in Figure 10. An example of how the hypothetical unit cell volumes of the subunits are determined is found in Figure S5. Based on Figure 10, the subunits within  $\text{Ce}_4\text{Fe}_3\text{Ge}_{10}$  and  $\text{Ce}_5\text{Co}_4\text{Ge}_{13}$  would still fall within the Kondo and magnetically ordering region, respectively.  $\text{Ce}_4\text{Fe}_3\text{Ge}_{10}$  only has one magnetic ordering ( $T_N \sim 3.7 \text{ K}$ ), while  $\text{Ce}_{n+1}\text{Co}_n\text{Ge}_{3n+1}$  analogues have multiple magnetic transitions.<sup>22–24</sup> Assuming the more complex magnetic ordering in the  $\text{Ce}_{n+1}\text{Co}_n\text{Ge}_{3n+1}$  analogues is due to the ground state of  $\text{CeCoGe}_3$ , this would mean that the magnetic ordering is due to (i) the interaction between the  $\text{CeFeGe}_3$  and the  $\text{CeFeGe}_2$  sublattice or (ii) the  $\text{CeFeGe}_2$ .

**4.1.2. CeNiSi<sub>2</sub> Electronic Landscape.** Doped compounds that reach a QCP fall within the crossover region; however, compared with the mapped Ce- $\text{BaNiSn}_3$  electronic landscape,

the crossover region for the Ce- $\text{CeNiSi}_2$  compounds is not linear. Such behavior may be due to effects caused by the transition metal vacancies. Nevertheless, we observe a trend similar to that in  $\text{BaNiSn}_3$ : (i) the distance between a magnetically ordering compound and the crossover region is correlated to the pressure necessary to induce superconductivity. Due to the lattice mismatch between the subunits, we observe an expansion of the  $\text{CeFeGe}_2$  subunit within the homologous series. The  $\text{CeFeGe}_2$  ( $V \sim 331 \text{ \AA}^3$ ) subunit present in  $\text{Ce}_4\text{Fe}_3\text{Ge}_{10}$  is located diagonally with respect to the parent structures due to an increment in volume and VEC toward the magnetically ordered regime, as shown in Figure 11. We searched for Ce analogues of the  $\text{Ln}_{n+1}\text{M}_n\text{X}_{3n+1}$  series ( $\text{Ln} = \text{lanthanide}$ ,  $\text{M} = \text{transition metal}$ ,  $\text{X} = \text{tetrel}$ ) to further validate the trends observed in the  $\text{CeNiSi}_2$  analogues and their relationship to the series.  $\text{Ce}_3\text{Ni}_2\text{X}_7$  ( $X = \text{Ge, Sn}$ )<sup>87,88</sup> and  $\text{Ce}_3\text{Co}_2\text{Sn}_7$ <sup>89</sup> are also members of the  $\text{Ln}_{n+1}\text{M}_n\text{X}_{3n+1}$  series with Ce1 and Ce2 in a local environment resembling the  $\text{AuCu}_3$  and the  $\text{CeNiSi}_2$  structure types, respectively. Through magnetic susceptibility and/or neutron diffraction, the magnetic ordering in  $\text{Ce}_3\text{Ni}_2\text{X}_7$  ( $X = \text{Ge, Sn}$ )<sup>87,88</sup> and  $\text{Ce}_3\text{Co}_2\text{Sn}_7$ ,<sup>89</sup> 7.2, 3.8, and 4.6 K, respectively, were attributed to the Ce2 sites. If we locate the corresponding  $\text{CeNiSi}_2$  analogues within Figure 11 and consider both the expansion of the subunit and the larger VEC due to the filling of the vacancies, then we can conclude that the subunits will be within the magnetically ordered regime.

We have rationalized the emergent magnetic ordering in  $\text{Ce}_4\text{Fe}_3\text{Ge}_{10}$  from two nonmagnetic parent structures,  $\text{CeFe}_{0.63}\text{Ge}_2$  and  $\text{CeFeGe}_3$ , through the understanding of the structural changes caused by the stacking of each subunit while also understanding the electronic landscape of the Ce analogues adopting the  $\text{BaNiSn}_3$  and  $\text{CeNiSi}_2$  structure types. The magnetic ordering within the structure seems to arise from the  $\text{CeFeGe}_2$  subunit's expansion, while the contraction of the  $\text{CeFeGe}_3$  subunit further enhances the Kondo interaction. Further studies, such as neutron diffraction, will be necessary to confirm the current hypothesis.

## 5. CONCLUSION

The new  $\text{Ce}_4\text{Fe}_3\text{Ge}_{10}$  has been reported and characterized through powder and single-crystal X-ray diffraction. It crystallizes in the  $Cmcm$  space group,  $\text{Eu}_2\text{Ni}_{2-x}\text{Sn}_5$  structure type, with lattice parameters of  $a = 4.3323 (15) \text{ \AA}$ ,  $b = 35.507 (9) \text{ \AA}$ , and  $c = 4.3069 (12) \text{ \AA}$ . We have established the Kondo and RKKY-interaction dominant regions for the Ce analogues adopting the  $\text{BaNiSn}_3$  and  $\text{CeNiSi}_2$  by plotting the unit cell volume as a function of VEC. To elucidate the emergent magnetism in comparison to the subunits, we located the new position of the subunits within the established electronic landscapes, determining that the  $\text{CeFeGe}_3$  contracts and falls within the Kondo-interaction dominant region, while the  $\text{CeFeGe}_2$  subunit is in the RKKY-interaction dominant region, therefore speculating the emergent magnetism arises from the  $\text{CeFeGe}_2$  subunit.

The  $\text{Ln}_{n+1}\text{M}_n\text{X}_{3n+1}$  ( $\text{Ln} = \text{lanthanide}$ ,  $\text{M} = \text{transition metal}$ ,  $\text{X} = \text{tetrel}$ ) homologous series provides an excellent opportunity to study structure property. The Ce-based  $\text{BaNiSn}_3$  and  $\text{CeNiSi}_2$  electronic landscapes in this article will guide the growth of the analogues within the region of interest. We foresee their use in the design of new analogues and doping studies to reach quantum critical points or superconductivity. The electronic landscape also highlights the potential of the

$\text{Ln}_{n+1}\text{M}_n\text{X}_{3n+1}$  (Ln = lanthanide, M = Co, Rh, Ir, X = tetrel) homologous series for high-pressure studies, where lower pressure may be necessary to reach superconductivity or a QCP in comparison to its subunits, while also providing potential for the design of spintronic through the tuning of the stacked subunits. A similar design principle through “strain engineering” can span to intermetallic families of materials with structural motifs related to the  $\text{BaAl}_4$ ,  $\text{AuCu}_3$ , and  $\text{CeNiSi}_2$  structure types. Potential structure types are the  $\text{Eu}_2\text{Pt}_7\text{AlP}_{3-x}$ ,<sup>33</sup>  $\text{U}_3\text{Co}_4\text{Ge}_7$ ,<sup>90</sup>  $\text{CePd}_n\text{Al}_m$ ,<sup>91</sup> and  $\text{Th}_2(\text{Au}_x\text{Si}_{1-x})\text{-}[\text{AuAl}_2]_n\text{Si}_2$ ,<sup>92</sup> since structural motifs related to  $\text{BaNiSn}_3$  and  $\text{CeNiSi}_2$  are part of their structure.

As Prof. DiSalvo noted in his manuscript, “...we find that as materials become more complex in stoichiometry and structure, new, interesting, and perhaps useful, phenomena are encountered.”<sup>93</sup> “While it is clear that some properties and phenomena depend critically on scale and processing, others depend on the complexity of the compound. But it is not at all clear what fraction of complex structures will support enhanced or novel phenomena rather than be uninteresting “bricks” truly is exemplified in modern materials.”<sup>93</sup> We envision the work presented in this manuscript is a step toward Prof. DiSalvo’s vision by understanding the constituent “chemical bricks” of a seemingly complex structure and the impact in properties stacking in bulk have. The work presented in this paper exemplifies the potential of rational design of complex structures and the associated novel phenomena by understanding the constituent “chemical bricks” and showcasing stacking as a tuning parameter.

## ■ ASSOCIATED CONTENT

### SI Supporting Information

The Supporting Information is available free of charge at <https://pubs.acs.org/doi/10.1021/acs.chemmater.4c01938>.

Figure S1 contains a Laue backscattering image of  $\text{Ce}_4\text{Fe}_3\text{Ge}_{10}$  along the [010]; Figures S2 and S3 show the local environments of Ce1 and Ce2 of  $\text{Ce}_4\text{Fe}_3\text{Ge}_{10}$  in comparison with the Ce local environments in  $\text{CeFeGe}_3$  and  $\text{CeFe}_{0.63}\text{Ge}_2$ , respectively; Figure S4 contains a general Doniach diagram; Figure S5 shows a hypothetical unit cell of the  $\text{CeFeGe}_3$  and  $\text{CeFeGe}_2$  subunits in  $\text{Ce}_4\text{Fe}_3\text{Ge}_{10}$  used to calculate the volumes used for Figures 10 and 11 in the manuscript; Tables S1 and S2 contain lattice parameters and magnetic properties of Ce-Ba $\text{NiSn}_3$  and Ce-Ce $\text{NiSi}_2$  analogues used for Figures 10 and 11 in the manuscript (PDF)

## Accession Codes

The single crystal X-ray crystallographic information file (CIF) for  $\text{Ce}_4\text{Fe}_3\text{Ge}_{10}$  is available at the Cambridge Crystallographic Data Centre with the deposition number: CCDC 2344170.

## ■ AUTHOR INFORMATION

### Corresponding Author

Julia Y. Chan – Department of Chemistry and Biochemistry, Baylor University, Waco, Texas 76798, United States; [orcid.org/0000-0003-4434-2160](https://orcid.org/0000-0003-4434-2160); Email: [Julia\\_Chan@baylor.edu](mailto:Julia_Chan@baylor.edu)

### Authors

Alexis Dominguez Montero – Department of Chemistry and Biochemistry, Baylor University, Waco, Texas 76798, United States

Sebastian A. Stoian – Department of Chemistry, University of Idaho, Moscow, Idaho 83844, United States; [orcid.org/0000-0003-3362-7697](https://orcid.org/0000-0003-3362-7697)

Gregory T. McCandless – Department of Chemistry and Biochemistry, Baylor University, Waco, Texas 76798, United States

Ryan E. Baumbach – Department of Physics, University of California, Santa Cruz, California 95064, United States

Complete contact information is available at: <https://pubs.acs.org/10.1021/acs.chemmater.4c01938>

## Notes

The authors declare no competing financial interest.

## ■ ACKNOWLEDGMENTS

J.Y.C. and A.D.M. acknowledge DOE-DE-SC0022854, NSF-DMR 2209804, and Welch AA-2056-20240404 for partial support of this work. R.E.B. acknowledges that a portion of this work was performed at the National High Magnetic Field Laboratory, which is supported by National Science Foundation Cooperative Agreement No. DMR-2128556 and the State of Florida. S.A.S. acknowledges the donors of the ACS Petroleum Research Fund for support of this research through a DNI grant to S.A.S. (62278-DNI3).

## ■ REFERENCES

- Thompson, J. D.; Movshovich, R.; Fisk, Z.; Bouquet, F.; Curro, N. J.; Fisher, R. A.; Hammel, P. C.; Hegger, H.; Hundley, M. F.; Jaime, M.; Pagliuso, P. G.; Petrovic, C.; Phillips, N. E.; Sarrao, J. L. Superconductivity and Magnetism in a New Class of Heavy-Fermion Materials. *J. Magn. Magn. Mater.* **2001**, *226–230*, 5–10.
- Buschow, K. H. J.; de Wijn, H. W.; van Diepen, A. M. Magnetic Susceptibilities of Rare-Earth–Indium Compounds:  $\text{RIn}_3$ . *J. Chem. Phys.* **1969**, *50*, 137–141.
- Lonzarich, G. G.; Mathur, N. D.; Grosche, F. M.; Julian, S. R.; Walker, I. R.; Freye, D. M.; Haselwimmer, R. K. W. Magnetically Mediated Superconductivity in Heavy Fermion Compounds. *Nature* **1998**, *394*, 39–43.
- Flouquet, J.; Haen, P.; Lejay, P.; Morin, P.; Jaccard, D.; Schweizer, J.; Vettier, C.; Fisher, R. A.; Phillips, N. E. Magnetic Instability in Ce Heavy Fermion Compounds. *J. Magn. Magn. Mater.* **1990**, *90–91*, 377–382.
- Petrovic, C.; Pagliuso, P. G.; Hundley, M. F.; Movshovich, R.; Sarrao, J. L.; Thompson, J. D.; Fisk, Z.; Monthoux, P. Heavy-Fermion Superconductivity in  $\text{CeCoIn}_5$  at 2.3 K. *J. Phys.: Condens. Matter* **2001**, *13*, L337.
- Petrovic, C.; Movshovich, R.; Jaime, M.; Pagliuso, P. G.; Hundley, M. F.; Sarrao, J. L.; Fisk, Z.; Thompson, J. D. A New Heavy-Fermion Superconductor  $\text{CeIrIn}_5$ : A Relative of the Cuprates? *Europhys. Lett.* **2001**, *53*, 354.
- Chen, G.; Ohara, S.; Hedo, M.; Uwatoko, Y.; Saito, K.; Sorai, M.; Sakamoto, I. Observation of Superconductivity in Heavy-Fermion Compounds of  $\text{Ce}_2\text{CoIn}_8$ . *J. Phys. Soc. Jpn.* **2002**, *71*, 2836–2838.
- Macaluso, R. T.; Sarrao, J. L.; Moreno, N. O.; Pagliuso, P. G.; Thompson, J. D.; Fronczek, F. R.; Hundley, M. F.; Malinowski, A.; Chan, J. Y. Single-Crystal Growth of  $\text{Ln}_2\text{MIn}_8$  (Ln = La, Ce; M = Rh, Ir): Implications for the Heavy-Fermion Ground State. *Chem. Mater.* **2003**, *15*, 1394–1398.
- Moshopoulou, E. G.; Sarrao, J. L.; Pagliuso, P. G.; Moreno, N. O.; Thompson, J. D.; Fisk, Z.; Ibberson, R. M. Comparison of the Crystal Structure of the Heavy-Fermion Materials  $\text{CeCoIn}_5$ ,  $\text{CeRhIn}_5$  and  $\text{CeIrIn}_5$ . *Appl. Phys. A: Mater. Sci. Process.* **2002**, *74*, s895–s897.
- Kumar, R. S.; Cornelius, A. L.; Sarrao, J. L. Compressibility of  $\text{CeMIn}_5$  and  $\text{Ce}_2\text{MIn}_8$  (M = Rh, Ir, and Co) compounds. *Phys. Rev. B* **2004**, *70*, No. 214526.

- (11) Weiland, A.; Felder, J. B.; McCandless, G. T.; Chan, J. Y. One Ce, Two Ce, Three Ce, Four? An Intermetallic Homologous Series to Explore:  $A_{n+1}B_nX_{3n+1}$ . *Chem. Mater.* **2020**, *32*, 1575–1580.
- (12) Hirose, Y.; Nishimura, N.; Honda, F.; Sugiyama, K.; Hagiwara, M.; Kindo, K.; Takeuchi, T.; Yamamoto, E.; Haga, Y.; Matsuura, M.; Hirota, K.; Yasui, A.; Yamagami, H.; Settai, R.; Ōnuki, Y. Magnetic and Superconducting Properties of CeRhGe<sub>2</sub> and CePtSi<sub>2</sub>. *J. Phys. Soc. Jpn.* **2011**, *80*, No. 024711.
- (13) Peter, S. C.; Chondroudi, M.; Malliakas, C. D.; Balasubramanian, M.; Kanatzidis, M. G. Anomalous Thermal Expansion in the Square-Net Compounds RE<sub>4</sub>TGe<sub>8</sub> (RE = Yb, Gd; T = Cr–Ni, Ag). *J. Am. Chem. Soc.* **2011**, *133*, 13840–13843.
- (14) Nikiforov, V. N.; Baran, M.; Jędrzejczak, A.; Irkhin, V. Y. Anomalous Ferromagnetism and Non-Fermi-Liquid Behavior in the Kondo Lattice CeRuSi<sub>2</sub>. *Eur. Phys. J. B* **2013**, *86*, 238.
- (15) Settai, R.; Sugitani, I.; Okuda, Y.; Thamizhavel, A.; Nakashima, M.; Ōnuki, Y.; Harima, H. Pressure-Induced Superconductivity in CeCoGe<sub>3</sub> Without Inversion Symmetry. *J. Magn. Magn. Mater.* **2007**, *310*, 844–846.
- (16) Honda, F.; Bonalde, I.; Yoshiuchi, S.; Hirose, Y.; Nakamura, T.; Shimizu, K.; Settai, R.; Ōnuki, Y. Pressure-Induced Superconductivity in Non-Centrosymmetric Compound CeIrGe<sub>3</sub>. *Physica C* **2010**, *470*, S543–S544.
- (17) Wang, H.; Guo, J.; Bauer, E. D.; Sidorov, V. A.; Zhao, H.; Zhang, J.; Zhou, Y.; Wang, Z.; Cai, S.; Yang, K.; Li, A.; Li, X.; Li, Y.; Sun, P.; Yang, Y.-f.; Wu, Q.; Xiang, T.; Thompson, J. D.; Sun, L. Superconductivity in Pressurized CeRhGe<sub>3</sub> and Related Non-centrosymmetric Compounds. *Phys. Rev. B* **2018**, *97*, No. 064514.
- (18) Pecharsky, V. K.; Hyun, O. B.; Gschneidner, K. A. Unusual Magnetic Properties of the Heavy-Fermion Compound CeCoGe<sub>3</sub>. *Phys. Rev. B* **1993**, *47*, 11839–11847.
- (19) Yamamoto, H.; Ishikawa, M.; Hasegawa, K.; Sakurai, J. CeFeGe<sub>3</sub>: A Concentrated Kondo Compound with a Stable Valency and High Kondo Temperature. *Phys. Rev. B* **1995**, *52*, 10136–10141.
- (20) Shimoda, T.; Okuda, Y.; Takeda, Y.; Ida, Y.; Miyachi, Y.; Kawai, T.; Fujie, T.; Sugitani, I.; Thamizhavel, A.; Matsuda, T. D.; Haga, Y.; Takeuchi, T.; Nakashima, M.; Settai, R.; Ōnuki, Y. Magnetic and Electronic Properties in CeTSi<sub>3</sub> and CeTGe<sub>3</sub> (T: Transition Metal). *J. Magn. Magn. Mater.* **2007**, *310*, 308–309.
- (21) François, M.; Venturini, G.; Malaman, B.; Roques, B. Nouveaux isotopes de CeNiSi<sub>2</sub> dans les systèmes R-M-X (R ≡ La-Lu, M ≡ métaux des groupes 7 A 11 ET X ≡ Ge, Sn). I Compositions et paramètres cristallins. *J. Less-Common Met.* **1990**, *160*, 197–213.
- (22) Weiland, A.; Wei, K.; McCandless, G. T.; Baumbach, R. E.; Chan, J. Y. Fantastic n = 4: Ce<sub>5</sub>Co<sub>4+x</sub>Ge<sub>13-y</sub>Sn<sub>y</sub> of the  $A_{n+1}M_nX_{3n+1}$  Homologous Series. *J. Chem. Phys.* **2021**, *154*, No. 114707.
- (23) Felder, J. B.; Weiland, A.; Hodovanets, H.; McCandless, G. T.; Estrada, T. G.; Martin, T. J.; Walker, A. V.; Paglione, J.; Chan, J. Y. Law and Disorder: Special Stacking Units—Building the Intergrowth Ce<sub>6</sub>Co<sub>5</sub>Ge<sub>16</sub>. *Inorg. Chem.* **2019**, *58*, 6037–6043.
- (24) Weiland, A.; Wei, K.; McCandless, G. T.; Felder, J. B.; Eddy, L. J.; Baumbach, R. E.; Chan, J. Y. Strongly Correlated Electron Behavior in a New Member of the  $A_{n+1}B_nX_{3n+1}$  Homologous Series: Ce<sub>7</sub>Co<sub>6</sub>Ge<sub>19</sub>. *Phys. Rev. Mater.* **2020**, *4*, No. 074408.
- (25) Doniach, S. The Kondo Lattice and Weak Antiferromagnetism. *Physica B+C* **1977**, *91*, 231–234.
- (26) Canfield, P. C.; Fisk, Z. Growth of Single Crystals From Metallic Fluxes. *Philos. Mag. B* **1992**, *65*, 1117–1123.
- (27) Canfield, P. C.; Kong, T.; Kaluarachchi, U. S.; Jo, N. H. Use of Frit-Disc Crucibles for Routine and Exploratory Solution Growth of Single Crystalline Samples. *Philos. Mag.* **2016**, *96*, 84–92.
- (28) Krause, L.; Herbst-Irmer, R.; Sheldrick, G. M.; Stalke, D. Comparison of Silver and Molybdenum Microfocus X-Ray Sources for Single-Crystal Structure Determination. *J. Appl. Crystallogr.* **2015**, *48*, 3–10.
- (29) Sheldrick, G. M. Crystal Structure Refinement with SHELXL. *Acta Crystallogr., Sect. C* **2015**, *71*, 3–8.
- (30) Yamamoto, H.; Sawa, H.; Ishikawa, M. A New Nonmagnetic Heavy-Electron Compound, CeFeGe<sub>3</sub>. *Phys. Lett. A* **1994**, *196*, 83–86.
- (31) Harmening, T.; Eul, M.; Pöttgen, R. Nickel-Deficient Stannides Eu<sub>2</sub>Ni<sub>2-x</sub>Sn<sub>3</sub> – Structure, Magnetic Properties, and Mössbauer Spectroscopic Characterization. *Z. Naturforsch. B* **2009**, *64*, 1107–1114.
- (32) Clark, W. P.; Ueltzen, K.; Burkhardt, U.; Akselrud, L.; Grin, Y.; Schwarz, U. High-Pressure High-Temperature Preparation of CeGe<sub>3</sub>. *Z. Naturforsch. B* **2023**, *78*, 189–193.
- (33) Lux, C.; Wenski, G.; Mewis, A. Eu<sub>2</sub>Pt<sub>7</sub>AlP<sub>~3</sub> und isotype Verbindungen: Eine neue Struktur aus CaBe<sub>2</sub>Ge<sub>2</sub><sup>-</sup> und Cu<sub>3</sub>Au-Einheiten/Eu<sub>2</sub>Pt<sub>7</sub>AlP<sub>~3</sub> und Isotypic Compounds: A New Structure Containing CaBe<sub>2</sub>Ge<sub>22</sub><sup>-</sup> and Cu<sub>3</sub>Au-Type Units. *Z. Naturforsch. B* **1991**, *46*, 1035–1038.
- (34) Makhaneva, A. Y.; Zakharova, E. Y.; Nesterenko, S. N.; Lyssenko, K. A.; Kuznetsov, A. N. Merging the AuCu<sub>3</sub>- and BaAl<sub>4</sub>-Based Structure Motifs: Flux-Assisted Synthesis, Crystal, and Electronic Structure of Ca<sub>2</sub>Pt<sub>7</sub>XP<sub>4-δ</sub> Phosphide Platinides (X = Al, Ti, and Zn). *Dalton Trans.* **2022**, *51*, 18583–18592.
- (35) Li, T.; Deng, S.; Liu, H.; Chen, J. Insights into Strain Engineering: From Ferroelectrics to Related Functional Materials and Beyond. *Chem. Rev.* **2024**, *124*, 7045–7105.
- (36) Oya, Y.; Mishima, Y.; Suzuki, T. The Pt-Al and Pt-Ga Phase Diagram With Emphasis on the Polymorphism of Pt<sub>3</sub>Al and Pt<sub>3</sub>Ga. *Int. J. Mater. Res.* **1987**, *78*, 485–490.
- (37) Bardi, U.; Ross, P. N. Superlattice Leed Patterns Observed from [111] and [100] Oriented Single Crystals of TiPt<sub>3</sub>. *Surf. Sci. Lett.* **1984**, *146*, L555–L560.
- (38) Nowotny, H.; Bauer, E.; Stempf, A.; Bittner, H. Über die Systeme: Platin-Zink und Platin-Kadmium. *Monatsh. Chem.* **1952**, *83*, 221–236.
- (39) Anderson, M. G.; Kyrk, T. M.; Idrees, M. Z.; Stoian, S. A.; McCandless, G. T.; Baumbach, R. E.; Chan, J. Y. Ironing out the Transition Metal Contribution to the Magnetism of the n = 3 Members of the Homologous Series Pr<sub>n+1</sub>M<sub>n</sub>Ge<sub>3n+1</sub> (M = Fe, Co): Pr<sub>4</sub>Fe<sub>3</sub>Ge<sub>10</sub> vs. Pr<sub>4</sub>Co<sub>3</sub>Ge<sub>10</sub>. *J. Alloys Compd.* **2024**, *976*, No. 172974.
- (40) Das, I.; Sampathkumaran, E. V.; Hirota, K.; Ishikawa, M. Kondo-Lattice Behavior of the Interstitial Alloys CeFe<sub>x</sub>Ge<sub>2</sub>. *Phys. Rev. B* **1994**, *49*, 3586–3588.
- (41) Kitagawa, J.; Muro, Y.; Takeda, N.; Ishikawa, M. Low-Temperature Magnetic Properties of Several Compounds in Ce-Pd-X (X = Si, Ge and Al) Ternary Systems. *J. Phys. Soc. Jpn.* **1997**, *66*, 2163–2174.
- (42) Muro, Y.; Eom, D.; Takeda, N.; Ishikawa, M. Contrasting Kondo-Lattice Behavior in CeTSi<sub>3</sub> and CeTGe<sub>3</sub> (T = Rh and Ir). *J. Phys. Soc. Jpn.* **1998**, *67*, 3601–3604.
- (43) Thamizhavel, A.; Takeuchi, T.; D Matsuda, T.; Haga, Y.; Sugiyama, K.; Settai, R.; Ōnuki, Y. Unique Magnetic Phases in an Antiferromagnet CeCoGe<sub>3</sub>. *J. Phys. Soc. Jpn.* **2005**, *74*, 1858–1864.
- (44) Okuda, Y.; Miyachi, Y.; Ida, Y.; Takeda, Y.; Tonohiro, C.; Oduchi, Y.; Yamada, T.; Duc Dung, N.; D Matsuda, T.; Haga, Y.; Takeuchi, T.; Hagiwara, M.; Kindo, K.; Harima, H.; Sugiyama, K.; Settai, R.; Ōnuki, Y. Magnetic and Superconducting Properties of LaIrSi<sub>3</sub> and CeIrSi<sub>3</sub> with the Non-Centrosymmetric Crystal Structure. *J. Phys. Soc. Jpn.* **2007**, *76*, No. 044708.
- (45) Kawai, T.; Okuda, Y.; Shishido, H.; Thamizhavel, A.; D Matsuda, T.; Haga, Y.; Nakashima, M.; Takeuchi, T.; Hedou, M.; Uwatoko, Y.; Settai, R.; Ōnuki, Y. Magnetic and Electrical Properties in CePtSi<sub>3</sub> Without Inversion Symmetry in the Crystal Structure. *J. Phys. Soc. Jpn.* **2007**, *76*, No. 014710.
- (46) Kawai, T.; Muranaka, H.; Measson, M.-A.; Shimoda, T.; Doi, Y.; D Matsuda, T.; Haga, Y.; Knebel, G.; Lapertot, G.; Aoki, D.; Flouquet, J.; Takeuchi, T.; Settai, R.; Ōnuki, Y. Magnetic and Superconducting Properties of CeTX<sub>3</sub> (T: Transition Metal and X: Si and Ge) with Non-Centrosymmetric Crystal Structure. *J. Phys. Soc. Jpn.* **2008**, *77*, No. 064716.
- (47) Hillier, A. D.; Adroja, D. T.; Manuel, P.; Anand, V. K.; Taylor, J. W.; McEwen, K. A.; Rainford, B. D.; Koza, M. M. Muon Spin

Relaxation and Neutron Scattering Investigations of the Non-centrosymmetric Heavy-Fermion Antiferromagnet CeRhGe<sub>3</sub>. *Phys. Rev. B* **2012**, *85*, No. 134405.

(48) Ueta, D.; Ikeda, Y.; Yoshizawa, H. Weak Ferromagnetism and Multiple Metamagnetic Transitions in the Non-Centrosymmetric Tetragonal Compound CePdSi<sub>3</sub>. *J. Phys. Soc. Jpn.* **2016**, *85*, No. 104703.

(49) Ueta, D.; Yoshida, M.; Ikeda, Y.; Liu, Y.; Hong, T.; Masuda, T.; Yoshizawa, H. Magnetic Structure of a Non-Centrosymmetric CePtSi<sub>3</sub>. *AIP Adv.* **2018**, *8*, 115006.

(50) Ueta, D.; Yoshida, M.; Kobuke, T.; Ikeda, Y.; Nakao, A.; Moyoshi, T.; Munakata, K.; Liu, Y.; Masuda, T.; Yoshizawa, H. Oval-Cycloidal Magnetic Structure with Phase-Shift in the Non-Centrosymmetric Tetragonal Compound CePdSi<sub>3</sub>. *J. Phys. Soc. Jpn.* **2021**, *90*, No. 114702.

(51) Ueta, D.; Yoshida, M.; Kobuke, T.; Ikeda, Y.; Masuda, T.; Yoshizawa, H. Complex Magnetic Phase Diagram in the Non-Centrosymmetric Compound CePtSi<sub>3</sub>. *J. Phys. Soc. Jpn.* **2021**, *90*, No. 064712.

(52) Rai, B. K.; O'Rourke, P.; Roy, U. N. Review on Crystal Structures and Magnetic Properties of RTX<sub>3</sub> Materials. *J. Phys.: Condens. Matter* **2022**, *34*, No. 273002.

(53) Venturini, G.; Malaman, B.; Meot-Meyer, M.; Fruchart, D.; Le Caer, G.; Malterre, D.; Roques, B. Structure and Magnetism of New Ternary Silicide RMnSi<sub>2</sub> (R = La-Sm) and RFeSi<sub>2</sub> (R = La-Nd). *Rev. Chim. Miner.* **1986**, *23*, 162–182.

(54) Das, I.; Sampathkumaran, E. V. Magnetic Behaviour of the Interstitial Alloys of the Type, CeM<sub>x</sub>Ge<sub>2</sub> (M = Fe, Co, Ni and Cu). *Solid State Commun.* **1992**, *83*, 765–770.

(55) Im, H. J.; Ito, T.; Miyazaki, H.; Kimura, S.; Kwon, Y. S.; Saitoh, Y.; Fujimori, S. I.; Yasui, A.; Yamagami, H. Fermi Surface Variation of Ce 4f-Electrons in Hybridization Controlled Heavy-Fermion Systems. *Solid State Commun.* **2015**, *209–210*, 45–48.

(56) Pelizzone, M.; Braun, H. F.; Muller, J. Magnetic Properties of RCoSi<sub>2</sub> Compounds (R = Rare Earth). *J. Magn. Magn. Mater.* **1982**, *30*, 33–36.

(57) Pecharsky, V. K.; Gschneidner, K. A. CeCo<sub>0.89</sub>Ge<sub>2</sub>: A Heavy-Fermion System. *Phys. Rev. B* **1991**, *43*, 8238–8244.

(58) Mun, E. D.; Lee, B. K.; Kwon, Y. S.; Jung, M. H. Kondo Ground State of CeCoGe<sub>2</sub>. *Phys. Rev. B* **2004**, *69*, No. 085113.

(59) Baumbach, R. E.; Lu, X.; Ronning, F.; Thompson, J. D.; Bauer, E. D. Quantum Criticality in CePt<sub>1-x</sub>Ni<sub>x</sub>Si<sub>2</sub>. *J. Phys.: Conf. Ser.* **2012**, *391*, No. 012006.

(60) Lu, J. J.; Mo, T. S.; Gan, K. J.; Lin, T. C.; Lee, M. K. Observation of RKKY-Kondo Competition and Non-Fermi-Liquid Behavior in the Intermetallic Compound Series Ce(Cu<sub>1-x</sub>Ni<sub>x</sub>)Si<sub>2</sub>. *J. Supercond. Novel Magn.* **2010**, *23*, 1473–1477.

(61) Lu, J. J.; Lee, M. K.; Jang, L. Y.; Tien, C. Evolution from Intermediate-Valence to Antiferromagnetic Kondo-Lattice Behavior in CeNi(Ge<sub>x</sub>Si<sub>1-x</sub>)<sub>2</sub>. *Solid State Commun.* **2005**, *135*, 25–29.

(62) Geibel, C.; Kämmerer, C.; Seidel, B.; Bredl, C. D.; Grauel, A.; Steglich, F. Magnetic Ordering in the Heavy-Fermion Compounds CePtSi<sub>2</sub> and CeNiGe<sub>2</sub>. *J. Magn. Magn. Mater.* **1992**, *108*, 207–208.

(63) Pikul, A. P.; Kaczorowski, D.; Bukowski, Z.; Plackowski, T.; Gofryk, K. Single-Crystal Study of Highly Anisotropic CeNiGe<sub>2</sub>. *J. Phys.: Condens. Matter* **2004**, *16*, 6119.

(64) Lee, W. H.; Shelton, R. N. Possibility of a Quartet Ground State of Cerium in a New Kondo Lattice Compound: CeCuSi<sub>2</sub>. *Solid State Commun.* **1988**, *68*, 443–446.

(65) Lu, J. J.; Lu, Y. M.; Lee, M. K.; Mo, T. S.; Jang, L. Y. Spin frozen in the Kondo-lattice compound: CeCuSi<sub>2</sub>. *J. Magn. Magn. Mater.* **2006**, *305*, 259–263.

(66) Gil, A.; Penc, B.; Gondek, Ł.; Szytuła, A.; Hernandez-Velasco, J. Crystal and Magnetic Structure of CeCu<sub>0.86</sub>Ge<sub>2</sub>. *J. Alloys Compd.* **2002**, *346*, 43–46.

(67) Rawat, R.; Das, I. Magnetic Transitions in CeCu<sub>0.86</sub>Ge<sub>2</sub> and PrCu<sub>0.76</sub>Ge<sub>2</sub> as Studied by Magnetocaloric Effect. *Phys. Rev. B* **2001**, *64*, No. 052407.

(68) Chevalier, B.; Rogl, P.; Hiebl, K.; Etourneau, J. On the Intermediate Valence of Ternary Silicides CeRhSi<sub>2</sub> and CeIrSi<sub>2</sub>. *J. Solid State Chem.* **1993**, *107*, 327–331.

(69) Kaczorowski, D.; Pikul, A. P.; Burkhardt, U.; Schmidt, M.; Ślebarski, A.; Szajek, A.; Werwiński, M.; Grin, Y. Magnetic Properties and Electronic Structures of Intermediate Valence Systems CeRhSi<sub>2</sub> and Ce<sub>2</sub>Rh<sub>3</sub>Si<sub>5</sub>. *J. Phys.: Condens. Matter* **2010**, *22*, No. 215601.

(70) Honda, F.; Yoshiuchi, S.; Hirose, Y.; Nakamura, T.; Yamamoto, E.; Tateiwa, N.; Haga, Y.; Takeuchi, T.; Settai, R.; Ōnuki, Y. Pressure-Induced Superconductivity in CePd<sub>3</sub>Al<sub>2</sub> and CeRhGe<sub>2</sub>, New Family of Heavy Fermion Superconductors. *Phys. Status Solidi B* **2010**, *247*, 617–620.

(71) Adroja, D. T.; Rainford, B. D. Antiferromagnetic Kondo lattice: CePdSi<sub>2</sub>. *Phys. B: Condens. Matter* **1997**, *230–232*, 762–765.

(72) Lu, J. J.; Tien, C.; Jang, L. Y. Evolution from Heavy-Fermion to Mixed-Valence Behavior in the Series CePt<sub>1-x</sub>Ir<sub>x</sub>Si<sub>2</sub>. *Solid State Commun.* **2001**, *120*, 29–33.

(73) Szlowska, M.; Griбанov, A.; Griбанova, S.; Kaczorowski, D. Antiferromagnetic Kondo Lattice CeIrGe<sub>2</sub>. *J. Alloys Compd.* **2018**, *735*, 855–860.

(74) Lu, J. J.; Lee, M. K.; Lu, Y. M.; Jang, L. Y. Observation of the Non-Fermi-Liquid Behavior in the Evolution from Heavy-Fermion to Valence-Fluctuation Behavior in Ce(Pt<sub>1-x</sub>Rh<sub>x</sub>)Si<sub>2</sub> Series. *J. Magn. Magn. Mater.* **2007**, *311*, 614–617.

(75) Lee, W. H.; Kwan, K. S.; Klavins, P.; Shelton, R. N. Crystal Structure, Resistivity, Magnetic Susceptibility and Heat Capacity of a New Dense Kondo System: CePtSi<sub>2</sub>. *Phys. Rev. B* **1990**, *42*, 6542–6545.

(76) Nakano, T.; Ohashi, M.; Oomi, G.; Matsubayashi, K.; Uwatoko, Y. Pressure-Induced Superconductivity in the Orthorhombic Kondo Compound CePtSi<sub>2</sub>. *Phys. Rev. B* **2009**, *79*, No. 172507.

(77) Griбанov, A.; Grytsiv, A.; Rogl, P.; Seropegin, Y.; Giester, G. X-Ray Structural Study of Intermetallic Alloys RT<sub>2</sub>Si and RTSi<sub>2</sub> (R = Rare Earth, T = Noble Metal). *J. Solid State Chem.* **2010**, *183*, 1278–1289.

(78) Xia, X.-B.; Shen, B.; Smidman, M.; Chen, Y.; Lee, H.; Yuan, H.-Q. Tuning the Heavy Fermion State of CeFeGe<sub>3</sub> by Ru Doping. *Chin. Phys. Lett.* **2018**, *35*, No. 067102.

(79) Skokowski, P.; Synoradzki, K.; Toliński, T. Comprehensive Studies of the Transformation Between Antiferromagnetic CeCoGe<sub>3</sub> and Heavy Fermion CeFeGe<sub>3</sub> Compounds. *J. Alloys Compd.* **2019**, *810*, No. 151850.

(80) Skokowski, P.; Synoradzki, K.; Werwiński, M.; Bajorek, A.; Chelkowska, G.; Toliński, T. Electronic Structure of CeCo<sub>1-x</sub>Fe<sub>x</sub>Ge<sub>3</sub> Studied by X-Ray Photoelectron Spectroscopy and First-Principles Calculations. *J. Alloys Compd.* **2019**, *787*, 744–750.

(81) Skokowski, P.; Synoradzki, K.; Reiffers, M.; Dzubinska, A.; Rols, S.; Arapan, S.; Legut, D.; Toliński, T. Effect of Transition Metals on the Crystal Field in CeCo<sub>0.4</sub>Fe<sub>0.6</sub>Ge<sub>3</sub>. *Intermetallics* **2023**, *153*, No. 107776.

(82) Krishnamurthy, V. V.; Nagamine, K.; Watanabe, I.; Nishiyama, K.; Ohira, S.; Ishikawa, M.; Eom, D. H.; Ishikawa, T.; Briere, T. M. Non-Fermi-Liquid Spin Dynamics in CeCoGe<sub>3-x</sub>Si<sub>x</sub> for x = 1.2 and 1.5. *Phys. Rev. Lett.* **2002**, *88*, No. 046402.

(83) Eom, D.; Takeda, N.; Ishikawa, M. Magnetic Instability Around the Quantum Critical Point in CeCoGe<sub>3-x</sub>Si<sub>x</sub> (0 ≤ x ≤ 3). *J. Phys. Soc. Jpn.* **2006**, *75*, No. 093706.

(84) Park, T.; Ronning, F.; Yuan, H. Q.; Salamon, M. B.; Movshovich, R.; Sarrao, J. L.; Thompson, J. D. Hidden Magnetism and Quantum Criticality in the Heavy Fermion superconductor CeRhIn<sub>5</sub>. *Nature* **2006**, *440*, 65–68.

(85) Paschen, S.; Si, Q. Quantum Phases Driven by Strong Correlations. *Nat. Rev. Phys.* **2021**, *3*, 9–26.

(86) Lai, Y.; Chan, J. Y.; Baumbach, R. E. Electronic Landscape of the f-Electron Intermetallics with the ThCr<sub>2</sub>Si<sub>2</sub> Structure. *Sci. Adv.* **2022**, *8*, No. eabp8264.

(87) Schobinger-Papamantellos, P.; André, G.; Rodríguez-Carvajal, J.; Buschow, K. H. J.; Durivault, L. Magnetic Ordering of CeNi<sub>0.78</sub>Sn<sub>2</sub>

and  $\text{Ce}_3\text{Ni}_2\text{Sn}_7$  Compounds by Neutron Diffraction. *J. Alloys Compd.* **2001**, 325, 29–36.

(88) Durivault, L.; Bourée, F.; Chevalier, B.; André, G.; Etourneau, J.; Isnard, O. Magnetic Structure of the Ternary Germanide  $\text{Ce}_3\text{Ni}_2\text{Ge}_7$ . *J. Magn. Magn. Mater.* **2001**, 232, 139–146.

(89) Chajewski, G.; Pasturel, M.; Pikul, A. P. Magnetic and Related Properties of a Novel Compound  $\text{Ce}_3\text{Co}_2\text{Sn}_7$ . *J. Alloys Compd.* **2017**, 706, 244–249.

(90) Pöttgen, R.; Chevalier, B.; Gravereau, P.; Darriet, B.; Jeitschko, W.; Etourneau, J. Crystal Structure and Magnetic Properties of the Ternary Germanide  $\text{U}_3\text{Co}_4\text{Ge}_7$ : An Intergrowth of  $\text{CaBe}_2\text{Ge}_2$ - and  $\text{Cu}_3\text{Au}$ -Type Slabs. *J. Solid State Chem.* **1995**, 115, 247–254.

(91) Tursina, A.; Khamitcaeva, E.; Griбанov, A.; Gnida, D.; Kaczorowski, D.  $\text{CePd}_2\text{Al}_2$ ,  $\text{CePd}_3\text{Al}_3$ , and  $\text{CePd}_4\text{Al}_4$ —A New Homologous Series Built of  $\text{CaBe}_2\text{Ge}_2$ - and  $\text{CsCl}$ -type Units. *Inorg. Chem.* **2015**, 54, 3439–3445.

(92) Lattturner, S. E.; Bilc, D.; Mahanti, S. D.; Kanatzidis, M. G. Quaternary Intermetallics Grown from Molten Aluminum: The Homologous Series  $\text{Th}_2(\text{Au}_x\text{Si}_{1-x})[\text{AuAl}_2]_n\text{Si}_2$  ( $n = 1, 2, 4$ ). *Chem. Mater.* **2002**, 14, 1695–1705.

(93) DiSalvo, F. J. Challenges and Opportunities in Solid-State Chemistry. *Pure Appl. Chem.* **2000**, 72, 1799–1807.



CAS BIOFINDER DISCOVERY PLATFORM™

## CAS BIOFINDER HELPS YOU FIND YOUR NEXT BREAKTHROUGH FASTER

Navigate pathways, targets, and  
diseases with precision

Explore CAS BioFinder

